PCCP

Cite this: *Phys. Chem. Chem. Phys.*, 2011, **13**, 3491–3501

www.rsc.org/pccp

PAPER

Enhanced photocatalytic activity of mesoporous TiO_2 aggregates by embedding carbon nanotubes as electron-transfer channel†

Jiaguo Yu,* Tingting Ma and Shengwei Liu

Received 10th July 2010, Accepted 5th November 2010
DOI: 10.1039/c0cp01139h

Mesoporous multiwalled carbon nanotubes/titanium dioxide ($CNTs/TiO_2$) nanocomposites with low loading amounts (0–0.5 wt%) of CNTs embedded inside mesoporous TiO_2 aggregates has been prepared by a simple one-pot hydrothermal method using titanium sulfate as titanium source. The as-prepared $CNTs/TiO_2$ samples are carefully characterized, analyzed and discussed. In contrast to previous reports with high CNT loading, our results indicate that a low CNT loading slightly influences the textural properties (including crystallite size, degree of crystallinity, specific surface areas, and pore volume *etc.*) and UV-light absorption of the mesoporous TiO_2 aggregates. The SEM and TEM results demonstrate that the CNTs are mostly embedded in the mesoporous TiO_2 aggregates. Moreover, chemical bonds are formed at the interface between CNTs and TiO_2, which is confirmed by the Raman, IR and XPS analyses. Significantly, we point out that PL analysis in terms of intensity of PL signals seems to not be a reliable way to monitor the recombination rate in the $CNTs/TiO_2$ composite, due to the quenching effect of CNTs. Instead, the analysis of transient photocurrent responses is introduced, which definitely reflects CNTs as fast electron transfer channels in chemically-bonded $CNTs/TiO_2$ composites with low CNT loading. Notably, the positive synergy effects of CNTs and TiO_2 depend on both the CNT loading amount and the state of interfacial contacts. In our study, only these chemically bonded $CNTs/TiO_2$ nanocomposites with appropriate loading amounts (<0.1 wt%) favor the separation of photogenerated electron-hole pairs and decrease their recombination rate and thus display significantly enhanced photocatalytic activity for degrading acetone in air under UV irradiation, as compared with pristine TiO_2 counterparts and commercial P25 photocatalyst. In contrast, a high CNT loading (>0.1 wt%) results in a decrease in photocatalytic activity; a simple mechanical mixing of CNTs and TiO_2 without forming chemical bonds at the interface also results in inferior photocatalytic performance.

1. Introduction

In order to dispose of environmental pollution, different methods have been exploited, such as adsorption,[1] biodegradation,[2] *etc*. In recent years, heterogeneous semiconductor photocatalysis has emerged as an advanced green technology. It has been extensively studied for environmental purification with emphasis on developing highly active oxide semiconductor photocatalysts.[3,4] To date, titania has proven to be the most suitable photocatalyst, largely due to its strong oxidizing power, biological and chemical inertness, avirulence and low cost.[5–10] Unfortunately, the photocatalytic performance of pure titania is still not good enough for industrial purposes. The high rate of photo-generated electron-hole recombination in TiO_2 particles results in low efficiency of photocatalysis. To date, a variety of strategies have been employed to improve the photocatalytic performance of TiO_2, for example, textural design,[11,12] doping,[13–17] and coupling TiO_2 with metal or other semiconductors,[18–24] *etc*. In particular, great interest has been devoted to combining carbon nanotubes (CNTs) with TiO_2 to enhance its photocatalytic performance.

CNTs attract considerable attention due to their special structure, large specific surface area, hollow and layered structures, extraordinary mechanical and unique electronic properties and their potential applications.[25] Especially, they have a large electron-storage capacity (one electron for every 32 carbon atoms),[26] and exhibit metallic conductivity similar to metals. Taking account of their good and controllable electrical characteristics and compatible band line-ups with TiO_2, it is believed that the composite of $CNTs/TiO_2$ is helpful

State Key Laboratory of Advanced Technology for Material Synthesis and Processing, Wuhan University of Technology, Luoshi Road 122#, Wuhan 430070, P. R. China. E-mail: jiaguoyu@yahoo.com

† Electronic supplementary information (ESI) available: One figure showing comparison of UV-vis diffuse reflection spectra of $MWCNTs/TiO_2$ nanocomposite samples with loadings of 0, 0.05, 0.1, 0.25, 0.5 and 10 wt% MWCNTs and pure MWCNTs. See DOI: 10.1039/c0cp01139h

This journal is © the Owner Societies 2011

for separating the photo-generated electron-hole pairs at the CNTs/TiO_2 interface,[27] and thus enhancing the photocatalytic performance. Later, experimental studies confirmed this point. For example, Yu *et al.*[7] demonstrated that CNTs/TiO_2 composites prepared by ultrasonic irradiation showed high photocatalytic activity toward decomposing gaseous acetone in air as well as azo dyes in aqueous solution. Subsequently, rapid developments were achieved regarding advanced synthetic techniques for reasonable structural design and improved photocatalytic activity of CNTs/TiO_2 composites. Notably, due to the low cost and simpler manipulation, hydrothermal synthesis is well developed using various titanium-based sources, such as titanium alkoxides, $(R–O–)_4Ti$ (*e.g.* titanium isopropoxide,[28,29] titanium butoxide[30,31] and titanium ethoxide),[32] titanium tetrafluoride,[33] titanium tetrachloride,[34] *etc.* However, many technical issues still remain. For instance, phase detachment between TiO_2 and CNTs, serious agglomeration, nonuniform crystallite and pore sizes are common drawbacks. In this regard, continuous efforts are still required to find an alternative synthetic route for TiO_2/CNT composites with a specific texture. In addition, it is noted that the loading amount of CNTs within the TiO_2 host is relatively high (usually more than 5 wt%) in the previous reports. A high CNT loading may bring some problems. Firstly, due to the interweavement of CNTs, a high CNT loading may result in a worse dispersion among the TiO_2 host. Secondly, the high CNT loading may largely shield the TiO_2 from absorbing the UV light (see electronic supplementary information (ESI), Fig. S1†). Moreover, the high CNT loading may exert significant influence over the textural, optical and adsorption features that are all affecting the photocatalytic activity. In this case, it is more difficult to clarify the dominant role of CNT loading in modifying the photocatalytic performance.

In this study, we choose titanium sulfate ($Ti(SO_4)_2$) as titanium source and develop a simple one-pot hydrothermal route to synthesize multi-walled carbon nanotubes/titania nanocomposites (MWCNTs/TiO_2) with low MWCNTs loading (0–0.5 wt%). The MWCNTs are embedded in the mesoporous TiO_2 aggregates and act as 'electron transfer channel' to efficiently separate the photo-generated charge carriers. As a consequence, such MWCNTs/TiO_2 nanocomposites show superior photocatalytic activity in decomposing gaseous acetone in air.

2. Experimental

2.1 Materials

All chemicals were reagent-grade and distilled water was used in the whole experiment. Multi-walled carbon nanotubes (MWCNTs) were provided by Beijing Key Lab of Green Chemical Engineering and Technology, Tsinghua University, Beijing, P. R. China. For purification, the raw MWCNTs were firstly oxidized in a mixture of concentrated sulfuric acid (98%) and nitric acid (68%) with a volume ratio of 3 : 1 under ultrasonication for 10 h at 50–60 °C.[35] Then, the MWCNTs were filtered, washed several times with distilled water until pH = 7. The product was subsequently dried in vacuum at 60 °C and kept in a desiccator for further use. After acid treatment, most of the impurities were removed and several types of functional groups were produced on the surface of the MWCNTs, including hydroxyl groups, carboxyl groups and carbonyl groups.[35,36]

2.2 Synthesis of TiO_2 and MWCNTs/TiO_2 nanocomposites

The MWCNTs/TiO_2 nanocomposites were synthesized by hydrothermal method using titanium sulfate ($Ti(SO_4)_2$) as titanium source. Firstly, 50 mg acid-treated MWCNTs were dispersed in 100 mL of distilled water under ultrasonic shaking for several hours to obtain a well-dispersed MWCNT suspension with a concentration of 0.5 g L^{-1}. Then, a specific amount of the MWCNTs suspension was introduced into the 150 mL $Ti(SO_4)_2$ solution to achieve the designed mass ratios of MWCNTs to titania (0, 0.05, 0.1, 0.25 and 0.5 wt%). The final concentration of $Ti(SO_4)_2$ was 0.052 M and the pH values were about 1.5. After stirring for another 30 min, the mixed suspension was transferred to a 200 mL Teflon-lined autoclave. This autoclave was sealed and maintained at 160 °C for 5 h. After this hydrothermal reaction, the obtained white or grey precipitates were collected, washed thoroughly with distilled water, followed by a rinse in absolute ethanol, and then dried in a vacuum at 80 °C for 12 h. For comparison, 0.1 wt% MWCNTs/TiO_2 nanocomposites were also prepared by simple mechanical mixing of the pristine TiO_2 reference and 0.1 wt% MWCNTs without the hydrothermal process. In the text, we denote pristine TiO_2 reference (0 wt% MWCNTs) as sample 1; MWCNTs/TiO_2 nanocomposites with loadings of 0.05, 0.1, 0.25 and 0.5 wt% MWCNTs prepared by hydrothermal process are denoted as samples 2, 3, 4 and 5,

Table 1 Summary of the physicochemical properties of MWCNTs/TiO_2 nanocomposite samples[a]

Samples	CNTs (wt%)	Phase	Relative crystallinity	*ACS*/nm	S_{BET}/m^2 g^{-1}	*APS*/nm	V_p/cm^3 g^{-1}
1	0	A	1	9.6	170.4	4.47	0.22
2	0.05	A	0.93	9.5	171.4	4.55	0.23
3	0.1	A	0.90	9.3	172.5	4.67	0.23
4	0.25	A	0.88	9.2	175.0	4.76	0.25
5	0.5	A	0.87	9.2	176.1	5.33	0.27
6	0.1	A	—	9.6	183.1	4.10	0.21
MWCNTs	100	—	—	—	244.2	17.84	1.19

[a] A—anatase; *ACS*—average crystallite size; S_{BET}—specific surface area; *APS*—average pore size; V_p—pore volume; Relative crystallinity—the relative intensity of the diffraction peak from the anatase (101) plane (reference sample 1). Samples 1–5 were synthesized by one-pot hydrothermal method, and sample 6 was prepared by a simple mechanical mixing method.

This journal is © the Owner Societies 2011

respectively; MWCNTs/TiO_2 nanocomposites with a loading of 0.1 wt% MWCNTs prepared by mechanical mixing is denoted as sample 6 (see Table 1).

2.3 Characterization

Powder X-ray diffraction (XRD) patterns were obtained on a D/Max-RB X-ray diffractometer (Rigaku, Japan) with Cu Kα radiation (λ = 0.15418 nm) at a scan rate (2θ) of 0.05° s^{-1}. The accelerating voltage and the applied current were 40 kV and 80 mA, respectively. XRD was used to determine the identity of any phase present and their crystallite size. The average crystallite sizes were calculated according to the Scherrer formula ($d = 0.9\lambda/\beta \cos\theta$, where d, λ, β and θ are crystallite size, Cu Kα wavelength, full width at half maximum intensity and Bragg's diffraction angle, respectively). Morphology observation was performed on an S-4800 field emission scanning electron microscope (SEM, Hitachi, Japan). Transmission electron microscopy (TEM) and high-resolution transmission electron microscopy (HRTEM) observations were conducted by a Tecnai G^2 F20 S-TWIN microscope at an accelerating voltage of 200 kV. The Brunauer-Emmett-Teller specific surface areas (S_{BET}) and porous structures of the samples were analyzed by a Micromeritics ASAP 2020 nitrogen adsorption apparatus (USA). All of the samples were degassed at 160 °C before nitrogen adsorption measurements. The BET surface area was determined by a multipoint BET method using the adsorption data in the relative pressure (P/P_0) range of 0.05–0.3. The desorption isotherm was used to determine the pore size distribution *via* the Barret-Joyner-Halender (BJH) method, assuming a cylindrical pore model.[37] The nitrogen adsorption volume at the relative pressure (P/P_0) of 0.99 was used to determine the pore volume and average pore size. Raman spectra were recorded at room temperature using a micro-Raman spectrometer (Renishaw InVia) in the back-scattering geometry with a 514.5 nm Ar^+ laser as an excitation source. The Fourier transform infrared spectra (FTIR) of the samples were recorded on IRAffinity-1 FTIR spectrometer. X-Ray photoelectron spectroscopy (XPS) measurement was performed in an ultrahigh vacuum with a VG ESCALAB 210 electron spectrometer equipped with a multichannel detector. The spectra were excited using Mg Kα (1253.6 eV) radiation (operated at 200 W) of a twin anode in the constant analyzer energy mode with a pass energy of 30 eV. UV-visible absorbance spectra were obtained for the dry-pressed disk samples with a UV-visible spectrophotometer (UV-2550, Shimadzu, Japan). $BaSO_4$ was used as a reflectance standard in a UV-visible diffuse reflectance experiment. Photoluminescence (PL) spectra were measured at room temperature on a fluorescence spectrophotometer (F-7000, Hitachi, Japan). The excitation wavelength was 315 nm, the scanning speed was 1200 nm min^{-1}, and the PMT voltage was 700 V. The width of the excitation slit and emission slit were both 5.0 nm.

2.4 Evaluation of photocatalytic activity

It is well known that volatile organic compounds (VOCs) are triggering serious environmental problems such as stratospheric ozone depletion and tropospheric ozone increase, depending on their chemical structures.[38,39] Acetone is a common VOC, which is a major constituent of many household chemicals and frequently used as a solvent in the printing industry and in analytical laboratories.[7] The long-term inhalation of acetone may lead to health disorders, such as leukemia, nausea, headache and fatigue. Degradation of acetone in air is of great significance. Therefore, we chose acetone as a model contaminate chemical. Photocatalytic oxidation of acetone is based on the following reaction:[40–42]

$$CH_3COCH_3 + 4O_2 \rightarrow 3CO_2 + 3H_2O \quad (1)$$

The photocatalytic activity experiments of the as-prepared samples and Degussa P25 for oxidation of acetone in air were performed at ambient temperature using a 15 L photocatalytic reactor.[43] The weight of the photocatalyst used for each experiment was about 0.3 g. The powder photocatalyst was coated on three Petri dishes (9.0 cm) and dried in an oven at 100 °C for 2 h. These catalyst-coated dishes were sealed in the reactor and 15 ± 1 μL of acetone were injected into the reactor with a micro-syringe. After adsorption equilibrium, the initial concentration of acetone was held at 300 ± 20 ppm, which remained constant for about 5 min prior to UV-irradiation. The initial temperature was 25 ± 1 °C. Finally, a 15 W 365 nm UV lamp (6 cm above the dishes) in the reactor was switched on to trigger the photocatalytic reaction. Integrated UV intensity measured with a UV radiometer (UV-A, made in Photoelectric Instrument Factory of Beijing Normal University) was 2.9 ± 0.1 mW cm^{-2}. The analysis of acetone, carbon dioxide, and water vapor concentration in the reactor was conducted on line with a Photoacoustic Field Gas-Monitor (INNOVA Air Tech Instruments Model 1412). Each set of experiment was followed for 60 min under UV irradiation.

2.5 Photoelectrochemical measurements

Photocurrents were measured using an electrochemical analyzer (CHI660C Instruments) in a standard three-electrode system using the prepared samples as the working electrodes with an active area of *ca.* 0.5 cm^2, a Pt wire as the counter electrode, and Ag/AgCl (saturates KCl) as a reference electrode. A 300 W Xe arc lamp served as a UV-light source. The integrated light intensity measured with a UV radiometer (UV-A) was 25 mW cm^{-2}. 1 M Na_2SO_4 aqueous solution was used as the electrolyte. Working electrodes were prepared as follows: 0.2 g of photocatalyst (samples 1, 3 and 5) were ground with 0.06 g polyethylene glycol (PEG, molecular weight: 20 000) and 0.5 ml water to make a slurry. The slurry was then coated onto a 2 cm × 1.2 cm F-doped SnO_2-coated glass (FTO glass) electrode by the doctor blade method. After these electrodes were dried in an oven, they were calcined at 450 °C for 30 min. All investigated electrodes have a similar film thickness (10–11 μm).

3. Results and discussion

3.1 Phase structures and morphology

Fig. 1 shows the XRD patterns for MWCNTs/TiO_2 nanocomposites synthesized with different contents of MWCNTs as compared with the acid-treated MWCNTs and pure TiO_2. As for MWCNTs/TiO_2 nanocomposites, the present peaks at

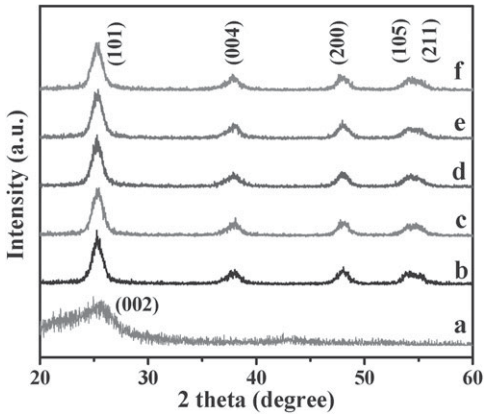

Fig. 1 XRD patterns of CNTs (a), samples 1 (b), 2 (c), 3 (d), 4 (e) and 5 (f).

25.3° (101), 37.8° (004), 48.1° (200), 54.0° (105), and 55.1° (211) clearly represent the formation of anatase (JCPDS no. 21-1272) crystallites. Otherwise, no apparent peaks for MWCNTs were observed. The trace amount of loaded MWCNTs with low atomic number (Z) cannot be resolved by XRD. Moreover, the intense (002) peak of MWCNTs is largely overlapped with the anatase (101) peak. However, the existence of MWCNTs can be clearly elucidated by Raman analysis as discussed later. Typically, the full width at half maximum (FWHM) of the anatase peaks for MWCNTs/TiO_2 nanocomposites are slightly broadened with an increasing amount of MWCNTs. Such a FWHM broadening suggests a decrease in the size of anatase crystallite. In the present case, taking account of possible interference from the MWCNTs over the anatase (101) peak, the anatase TiO_2 (200) reflection plane (2θ = 48.1°) was selected to estimate crystallite sizes based on FWHM broadening using the Scherrer formula. As shown in Table 1, the average crystallite size for pure TiO_2 is *ca*. 9.6 nm, while that for the MWCNTs/TiO_2 nanocomposites slightly decrease from 9.5 to 9.2 with increasing loading of MWCNTs from 0.05 to 0.5 wt%. This result suggests that the presence of the MWCNTs in the MWCNTs/TiO_2 nanocomposites hinders the anatase crystallite growth. Moreover, the crystallinity of TiO_2 in the MWCNTs/TiO_2 nanocomposites is impaired by loading MWCNTs, especially with higher content (see Table 1).

The external morphology and microstructures of MWCNTs/TiO_2 nanocomposites loaded with 0.1 wt% CNTs (sample 3) are further studied by SEM and TEM relative to MWCNTs. The TEM image (Fig. 2a) of MWCNTs shows its typical multi-walled tube-like profiles, and the diameter is *ca*. 10 nm. In the case of MWCNTs/TiO_2 nanocomposites, due to preferential heterogeneous nucleation, a very uniform shell consisting of tiny TiO_2 nanoparticles (Fig. 2b), deposits on the MWCNTs, whose surface contains an abundance of hydroxyl groups, carboxyl groups and carbonyl groups. Such a textual feature is further confirmed by the corresponding TEM investigation (Fig. 2c). Notably, the typical diameter of MWCNTs/TiO_2 nanocomposites significantly increases up to 60 nm (Fig. 2c). With progressive nucleation and growth, such preformed one-dimensional MWCNTs/TiO_2 nanocomposites are further embedded in TiO_2 aggregates (Fig. 2b and c). Fig. 2d gives the corresponding HRTEM image. It shows clear lattice fringes for the identification of crystallographic spacing. The fringe spacing of *ca*. 0.351 and 0.338 nm matches well with the TiO_2 (101) plane and the MWCNT (002) plane, respectively. This implies that there is a good contact between MWCNTs and TiO_2 particles. MWCNTs are directly coupled with the uniform anatase shell, which are together embedded in the TiO_2 aggregates. Such a structural feature is beneficial for efficient electron transfer and hole-electron separation, as if there is a 'conducting wire' acting as a readily accessible electron-transfer channel.

3.2 BET surface areas and pore size distributions

The porous structures and BET surface areas of as-prepared MWCNTs/TiO_2 nanocomposites are investigated based on the nitrogen sorption measurement. Fig. 3 shows the nitrogen sorption isotherms and the corresponding pore size distribution curves for samples 1, 3, 5 and MWCNTs. As for pure TiO_2 (sample 1), the isotherms are of type IV (BDDT classification) with a typical hysteresis loop, associated with capillary condensation of gases within mesopores (2–50 nm).[37,44] This hysteresis loop typically belongs to type H2, consistent with pores with narrow necks and wider bodies (ink-bottle pores).[44] The corresponding pore size distribution indicates that sample 1 contains non-uniform intra-aggregated mesopores with typical pore size ranging from 1.7 to 7.5 nm. Fig. 3b gives the N_2 sorption isotherm and the corresponding pore size distribution for MWCNTs. The H3-like loop is an indication of slit-like pores. The isotherms show high absorption at high relative pressure (P/P_0) range (approaching 1.0), indicating the formation of large mesopores and macropores. According to the morphology of MWCNTs observed in Fig. 2a, the smaller pores (<4 nm) correspond to the pores inside the nanotubes and the diameters of these pores are equal to the inner diameter of the nanotubes, while the larger pores (10–70 nm) can be attributed to the aggregation of the nanotubes.[45] Obviously, the pure TiO_2 and pristine MWCNTs exhibit distinct pore structures. In the case of MWCNTs/TiO_2 nanocomposites, due to the rather low MWCNT loading, the MWCNTs/TiO_2 nanocomposites (samples 3 and 5) exhibit rather similar N_2 sorption isotherms (Fig. 3a, inset) relative to the pure TiO_2 (sample 1), and exhibit comparable pore structures, as confirmed by the corresponding pore size distribution. The quantitative details about the BET surface areas, pore volumes and average pore diameter are listed in Table 1. MWCNTs have a large surface area (244.2 $m^2\ g^{-1}$) and a big pore volume. It is reasonable to conclude that with increasing content of MWCNTs, the S_{BET} and the pore volume of the composites increase slightly. It is expected that an increase in the S_{BET} and the pore volume leads to an increase in adsorption capacity of pollutants, which is beneficial for enhancing the photocatalytic activity.

3.3 Raman and IR spectra

Raman spectroscopy has been commonly applied to identify the local order characteristics of TiO_2.[7,46] Herein, the influence of MWCNTs loading on the local structure of anatase TiO_2 matrix is investigated by Raman spectra. Fig. 4 shows the

This journal is © the Owner Societies 2011

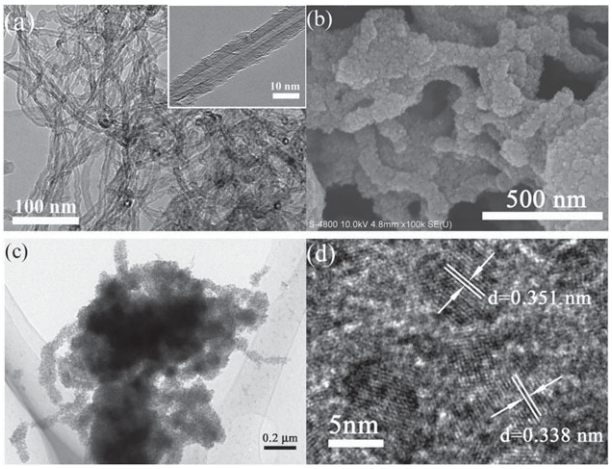

Fig. 2 TEM image of CNTs (a) and SEM (b), TEM (c), HRTEM (d) images of sample 3.

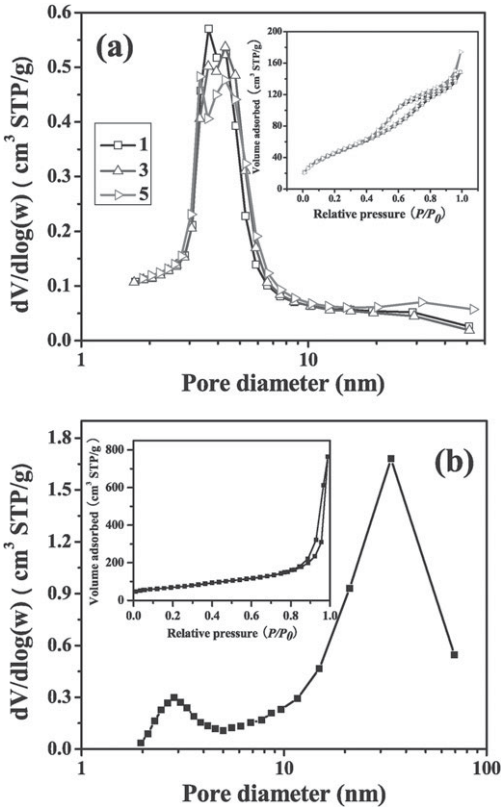

Fig. 3 N_2 adsorption–desorption isotherm and the corresponding pore-size distribution curves of samples 1, 3, 5 (a) and MWCNTs (b).

comparison of the Raman spectra of acid-treated MWCNTs, pure TiO_2 (sample 1) and MWCNTs/TiO_2 nanocomposites (samples 3 and 5). In the case of pure TiO_2 (Fig. 4a), characteristic bands at 150, 395.1, 512.5 and 636.7 cm^{-1} correspond to the $E_{g(1)}$, $B_{1g(1)}$, A_{1g} + $B_{1g(2)}$ and $E_{g(2)}$ modes of anatase, respectively.[46,47] As for acid-treated MWCNTs, there are two typical Raman bands (Fig. 4d). The band at around 1345 cm^{-1} is common for disordered sp^2 carbon and has been called the D-band.[48] The other band at around 1575 cm^{-1} is close to that observed for well ordered graphite

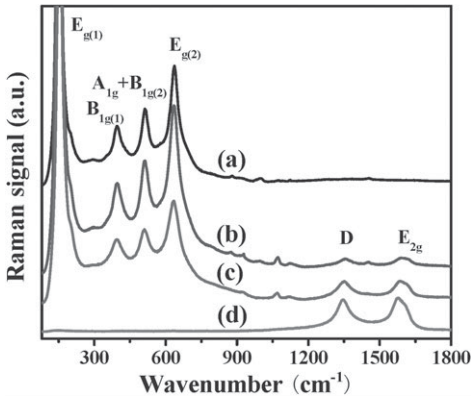

Fig. 4 Raman spectra of samples 1 (a), 3 (b), 5 (c) and MWCNTs (d).

and is often called as G-band or E_{2g} mode.[49] In the case of MWCNTs/TiO_2 nanocomposites (samples 3 and 5), all the Raman bands for anatase and MWCNTs still remain (Fig. 4b and c), except that the anatase Raman bands for MWCNTs/TiO_2 nanocomposites are slightly broadened as compared to the pure TiO_2 (sample 1). Such a peak broadening is consistent with their decease in the average crystallite size (Table 1 and Fig. 1). Significantly, it is reasonable to observe the two obvious peaks corresponding to MWCNTs in the Raman spectra for MWCNTs/TiO_2 nanocomposites. Also, with increasing MWCNT loading amount, those two peaks become strong. In addition, it is noteworthy that the peaks assigned to MWCNTs within the nanocomposites exhibit broadening and a slight blue-shift relative to acid-treated MWCNTs, indicating the interfacial interaction between TiO_2 and acid-treated MWCNTs.[7] Such a result further shows a real integration across the interface between MWCNTs and anatase, rather than a mere mixture.

Fig. 5 shows the IR spectra in the region of 500–2000 cm^{-1} for IR-active fundamental vibrations of TiO_2 and MWCNTs, as well as vibrations associated with surface adsorbates. Vibrations associated with surface adsorbed water (1640 cm^{-1}), CO_2 molecules (1120 cm^{-1}) and surface carbonate ions from CO_2 adsorption (1396 cm^{-1}) are observed for all the samples.[46] A weak band at 1040 cm^{-1} is assigned to the bending vibration of the hydroxyl group bound to coordinative

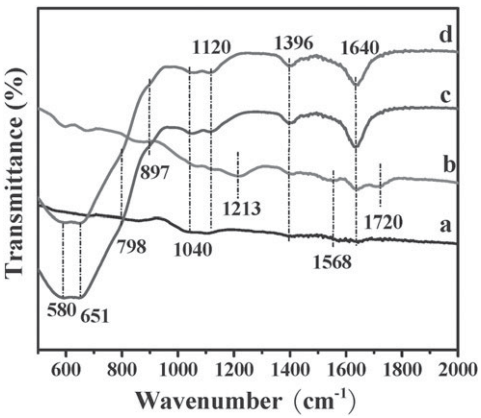

Fig. 5 IR spectra of pristine MWCNTs (a), acid-treated MWCNTs (b), samples 1 (c) and 3 (d).

unsaturated host surface atoms.[46] Both the pristine (Fig. 5a) and acid-treated MWCNTs (Fig. 5b) show a typical peak at 1568 cm^{-1}, associated with the IR active carbon stretching mode of nanotubes.[36,47,50] However, two new peaks emerge at 1720 and 1213 cm^{-1} for the acid-treated MWCNTs (Fig. 5b), which are related to the stretching vibration of carboxyl groups formed during treatment by the mixed acid.[36,47] It should be mentioned that these surface functional groups favor their dispersion in water and provide active sites for directed deposition of anatase nanocrystals around the surface of MWCNTs. The IR-active fundamental vibrations of TiO_2 appear in the 400–1000 cm^{-1} range. The intensive broad bands are ascribed to the stretching vibrations of Ti–O bonds (651 cm^{-1}) and Ti–O–Ti bonds (580 cm^{-1}).[46] The absorption in the spectral range of 700–1000 cm^{-1} (*e.g.* 798 and 897 cm^{-1}) is assigned with the surface vibrations originating from incorporating of water molecules or other ligand molecules to the coordination sphere of coordinate non-saturated surface Ti atoms (Fig. 5c and d).[46] When TiO_2 is immobilized on the sidewalls of MWCNTs, some covalent bonds (Ti–O–C═O or Ti–O–C) formed due to the esterification process between MWCNTs-COOH and TiO_2. As a result of the surface interaction between TiO_2 and MWCNTs, such surface vibrations of TiO_2 (798, 897 and 1040 cm^{-1}) were slightly weakened for MWCNTs/TiO_2 nanocomposites (sample 3) relative to pure TiO_2 (sample 1). Such IR results further confirm the real integration across the interface and chemically bonded interfacial contact between MWCNTs and TiO_2 nanoparticles.

3.4 XPS analysis

X-Ray photoelectron spectroscopy (XPS) measurements are performed to further elucidate the interaction between MWCNTs and TiO_2 nanoparticles. Fig. 6a shows the XPS survey spectrum for MWCNTs/TiO_2 nanocomposites loaded with 0.1 wt% MWCNTs (sample 3). As expected, it contains C, in addition to Ti and O, with sharp XPS peaks centered at binding energies of 459 (Ti 2p), 530 (O 1s) and 285 eV (C 1s). For analyzing the chemical nature of C, we examine the high-resolution XPS spectra of the C 1s region (Fig. 6b). The asymmetrical and broad features of C 1s XPS peaks suggest the coexistence of distinguishable models. A signal deconvolution after Gaussian curve fitting was shown in Fig. 6b, pointing out chemically variant C species in the TiO_2 matrix, with their C 1s binding energies at about 284.6, 285.3, 286.8 and 288.7 eV. The main C 1s peak at binding energy (BE) of 284.6 eV is assigned to adventitious carbon and sp^2-hybridized carbon from the MWCNTs.[33] The sharp peak located at 285.3 eV is known to be defect-containing sp^2-hybridized carbons.[51] Beside these two kinds of C–C bonds, there are two other weak peaks positioned at 286.8 and 288.7 eV, corresponding to hydroxyl carbon (C–O) and carboxyl carbon (O═C–O), respectively.[32,51] Such surface functional groups provide active sites for directed deposition of anatase nanocrystals around the surface of MWCNTs. For example, the –OH groups on the Ti precursor possibly react with the –OH and –COOH groups on the MWCNTs surface through esterification to form C–O–Ti or O═C–O–Ti bonds, as mentioned above.

3.5 UV-vis analysis

The optical properties of the as-prepared MWCNTs/TiO_2 nanocomposites (samples 2–5), together with pure TiO_2 (sample 1), have been measured by UV-vis diffuse reflectance spectra. As displayed in Fig. 7, all of these samples display the typical absorption with an intense transition in the UV region of the spectra, which is assigned to the intrinsic band gap absorption of TiO_2 due to the electron transitions from the valence band to conduction band ($O_{2p} \rightarrow Ti_{3d}$).[5,52] The pure TiO_2 (sample 1, Fig. 7a) shows no absorption above its fundamental absorption edge (around 400 nm). In contrast, the MWCNTs/TiO_2 nanocomposites (samples 2–5, Fig. 7b–e) exhibit increasing absorption in the visible region with an increasing loading amount of MWCNTs, which is in agreement with the color changing from white to grey (inset in Fig. 7). Further observation indicates that all the MWCNTs/TiO_2 nanocomposites have almost the same absorption edge as that of pure TiO_2, possibly ruling out the lattice doping of carbon into TiO_2 host. The previous investigation indicates that there is a significant change in the UV absorption observed for the MWCNTs/TiO_2 nanocomposites.[7,52] However, in the present case, there is almost no increase or decease in UV-light absorption found. This is due to the fact that the loading amount of MWCNTs (0–0.5 wt%) is low and, also, the loaded MWCNTs are mostly embedded inside the mesoporous aggregates (see Fig. 2 and S1†).

3.6 Photocatalytic activity

The photocatalytic activities of the as-prepared MWCNTs/TiO_2 nanocomposites were evaluated by the oxidation of acetone in air. However, under dark conditions without light illumination, the concentration of acetone showed no change for every measurement using the various TiO_2 samples. Illumination in the absence of TiO_2 samples did not result in the photocatalytic decomposition of acetone. Therefore, the presence of both illumination and TiO_2 was necessary for the efficient degradation. These results clearly indicated that the decomposition of acetone in air was caused by photocatalytic reactions on TiO_2 powders under UV illumination. As shown in Fig. 8a, with increasing UV-irradiation time, the concentration of acetone and carbon dioxide linearly decreases and increases, respectively, for all the selected photocatalysts. Moreover, the concentration of the produced carbon dioxide is about three times as much as that of the acetone destroyed. This result conforms to reaction (1), concluding that the acetone pollutant can be completely decomposed using all the selected photocatalysts under UV irradiation. In addition, it is clearly demonstrated that the MWCNTs/TiO_2 nanocomposites with loading of 0.1 wt% MWCNTs (sample 3) shows the best performance.

The photocatalytic activity of the catalysts can also be quantitatively evaluated by comparing the apparent reaction rate constants. On the basis of previous reports, the photocatalytic oxidation of acetone is a pseudo-first-order reaction when C_0 is low, and its kinetics can be expressed as: $\ln(C_0/C) = kt$,[9] where k is the apparent reaction rate constant, and C_0 and C are the initial and the reaction concentration of acetone, respectively. Fig. 8b displays the apparent rate

 This journal is © the Owner Societies 2011

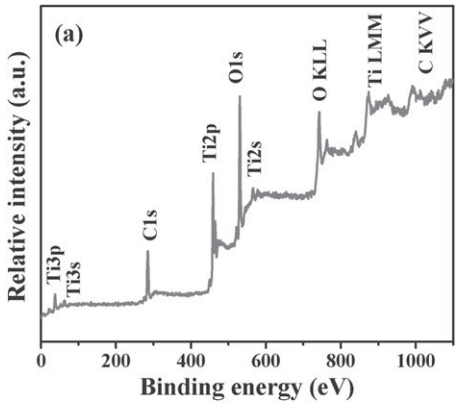

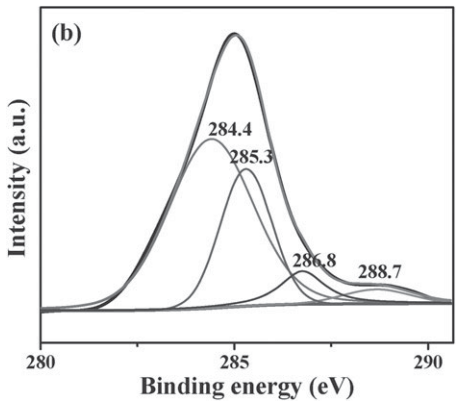

Fig. 6 XPS survey spectrum (a) and high-resolution C 1s XPS spectrum (b) of sample 3.

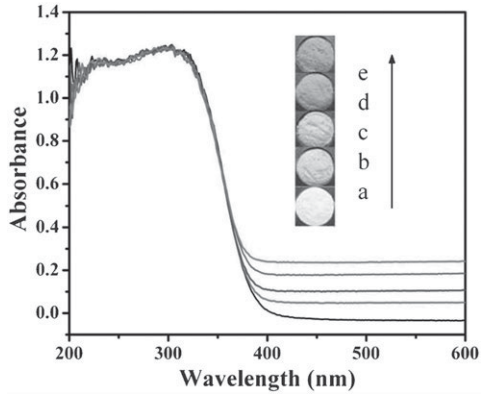

Fig. 7 UV-vis diffuse reflection spectra of samples 1 (a), 2 (b), 3 (c), 4 (d) and 5 (e).

constants (k) for the MWCNTs/TiO_2 nanocomposites prepared with different contents of MWCNTs in comparison with P25. The k value for P25 commercial photocatalyst is 5.06×10^{-3} under the same experimental conditions. Without MWCNTs, the pure TiO_2 sample (sample 1) shows a good photocatalytic activity and its k reaches 8.84×10^{-3}, owing to its anatase phase structure, high specific surface area and small crystallite size (see Table 1). The addition of MWCNTs exhibits a significant influence on the photocatalytic activity of the resulting MWCNTs/TiO_2 nanocomposites. Even with the addition of a small amount of MWCNTs (0–0.5 wt%), the

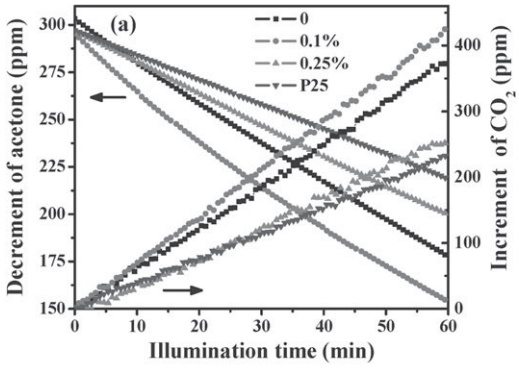

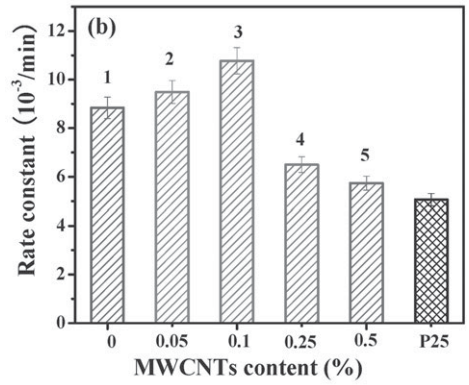

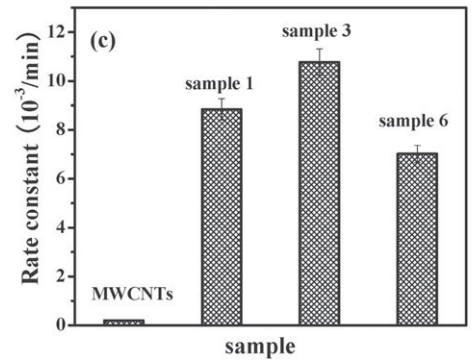

Fig. 8 (a) Concentration-time plots of acetone and carbon dioxide. (b) Photocatalytic activity comparison of samples 1–5 and P25. (c) Comparison of the apparent rate constants for acetone photodegradation on MWCNTs, samples 1, 3 and 6.

value of k varies greatly. Especially, the photocatalytic activity initially increases significantly with increasing embedded MWCNTs content (0.05 and 0.1 wt%), and the k reaches the highest value of 10.77×10^{-3} at 0.1 wt% MWCNTs (sample 3). In this regard, the photocatalytic activity of sample 3 exceeds that of P25 by a factor of 2.13. With further increasing MWCNTs content (0.25 and 0.5 wt%), although a better photocatalytic activity relative to P25 is still obtained for MWCNTs/TiO_2 nanocomposites (samples 4 and 5), a gradual decrease in the photocatalytic activity occurs. The decrease in photoactivity is related to the increased recombination rate of electron-hole pairs as a result of lower degree of crystallinity (Table 1). The present results are consistent with previous studies that a suitable loading content of MWCNTs is crucial for optimizing the photocatalytic activity of MWCNTs/TiO_2 nanocomposites.[7,28]

In addition, it should be noted that chemically bonded interfacial contact between TiO_2 and MWCNTs are also important for the enhancement of photocatalytic performance. For comparison, the photocatalytic activity of 0.1 wt% MWCNTs/TiO_2 composite prepared by a simple mechanical mixing method (sample 6) has also been tested and analyzed. As shown in Fig. 8c, a simple mechanical mixing process cannot produce an effective TiO_2/MWCNT composite photocatalyst, and even shows lower activity than pure TiO_2 (sample 1) for acetone degradation. In fact, this observation is consistent with the previous studies regarding both phenol degradation in the liquid phase and benzene degradation in the gas phase using CNTs/TiO_2 composite prepared by mechanical mixing.[52,53] It is proposed that a mechanical mixing process is not able to create effective interfacial contact between TiO_2 and CNTs. In this regard, the MWCNTs loading can not efficiently facilitate the interfacial electron transfer and electron-hole separation. Moreover, they may shield the UV-light adsorption of TiO_2 photocatalyst. Thus, the simple mechanical mixing of TiO_2 and MWCNTs without effective interfacial contact between them cannot enhance photocatalytic acetone decomposition but hinder it. In contrast, when there is a chemical bond and effective interfacial contact between TiO_2 and MWCNTs, the photocatalytic performance is significantly enhanced.

3.7 Origin of the enhancement of the photoactivity of MWCNTs/TiO_2 nanocomposites

In the previous studies, it is proposed that the introduction of MWCNTs within the TiO_2 host has multiple positive affects, including increasing the capacity of adsorption, tuning the range of light response, prolonging the recombination time of photo-generated charge carriers, *etc*., thus enhancing the photocatalytic performance. Herein, we discuss the dominant role of loading MWCNTs in modifying the photocatalytic performance of as-prepared MWCNTs/TiO_2 nanocomposites.

Firstly, although the specific surface area of MWCNTs is as high as 224.2 $m^2\ g^{-1}$, the fluctuation in specific surface areas ($175 \pm 5\ m^2\ g^{-1}$) for MWCNTs/TiO_2 nanocomposites with various loading amounts of MWCNTs is limited (Table 1). Owing to the low loading amount of MWCNTs (0–0.5 wt%), the contribution from MWCNTs themselves to the overall specific surface areas is negligible. The effect of MWCNTs on crystallite growth and thus specific surface areas is also limited (Table 1). In this regard, the variation in adsorption capacity (affected largely by the surface areas) is not the main reason for the enhancement of photoactivity of MWCNTs/TiO_2 nanocomposites.

Secondly, as for optical properties of MWCNTs/TiO_2 nanocomposites, although visible-light absorption increases with increasing loading amount of MWCNTs, there is almost no change in the UV-light absorption and no shift in the absorption edge. This is quite different from previous studies in that the UV-light absorption decreases at relatively high loading amounts of MWCNTs.[7,52] It is claimed that the high loading of MWCNTs can shield the UV light from being absorbed by TiO_2. However, the loading amount of MWCNTs is low in the present case, and more importantly, they are mostly embedded in the mesoporous TiO_2 aggregates. Subsequently, the effects of MWCNTs on the optical properties of TiO_2 host is limited to enhancing the visible-light absorption that can not be absorbed by TiO_2. The influence of embedded MWCNTs on the UV-light absorption is negligible (see Fig. 2 and Fig. S1†), and thus the variation in optical properties is also not the main reason for the enhancement of photoactivity of MWCNTs/TiO_2 nanocomposites.

Except for the limited effects to adsorption capacity and light-response mentioned above, the dominant contribution of MWCNTs in MWCNTs/TiO_2 nanocomposites to photoactivity is largely related to an increase in recombination time for photo-generated electron-hole pairs. A schematic illustration for the mechanism of enhanced photoactivity of the MWCNTs/TiO_2 nanocomposites is shown in Fig. 9. Under UV-light illumination, electrons (e^-) are excited from the valance band (VB) to the conduction band (CB) of anatase, creating holes (h^+) in the VB. Normally, these charge carriers quickly recombine and only a fraction of the electrons and holes participate in the photocatalytic reaction, resulting in a low reactivity.[53] However, when anatase nanoparticles are chemically bonded to the surface of MWCNTs, these photo-generated electrons tend to transfer to MWCNTs (eqn (2)), leading to hole-electron separation. These separated electrons and holes are then trapped by some surface adsorbates to generate highly reactive radical species. For example, the holes left in TiO_2 VB can react with adsorbed water (or surface hydroxyl) to form hydroxyl radicals ($^\bullet OH$) (eqn (3)). The electrons stored in MWCNTs are also trapped by O_2 to form very reactive superoxide radical ions ($^\bullet O_2^-$) (eqn (4)). Both radical groups ($^\bullet O_2^-$ and $^\bullet OH$) are highly reactive towards the degradation of the organic compounds, such as acetone used in the present study.

$$\text{MWCNTs/TiO}_2 \xrightarrow{h\nu} \text{MWCNTs}(e)/\text{TiO}_2(h) \qquad (2)$$

$$\text{TiO}_2(h) + {}^-\text{OH} \rightarrow \text{TiO}_2 + {}^\bullet\text{OH} \qquad (3)$$

$$\text{MWCNTs}(e) + \text{O}_2 \rightarrow \text{MWCNTs} + {}^\bullet\text{O}_2^- \qquad (4)$$

In the previous studies, photoluminescence (PL) analysis is commonly used to confirm the above proposition. Herein, we conduct PL measurements for the pure TiO_2 sample (sample 1) and composite TiO_2 samples prepared by hydrothermal method (samples 3 and 5) or mechanical mixing (sample 6),

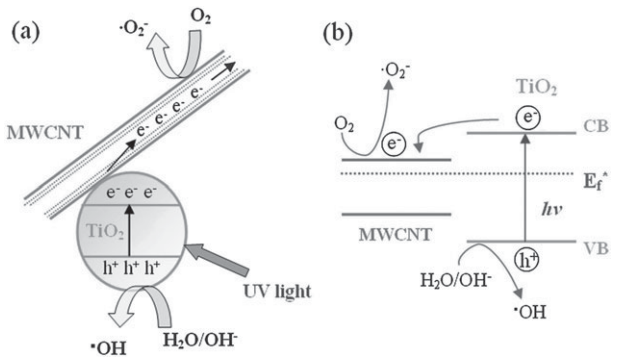

Fig. 9 Proposed mechanism for the enhanced electron transfer in the MWCNTs/TiO_2 nanocomposites.

 This journal is © the Owner Societies 2011

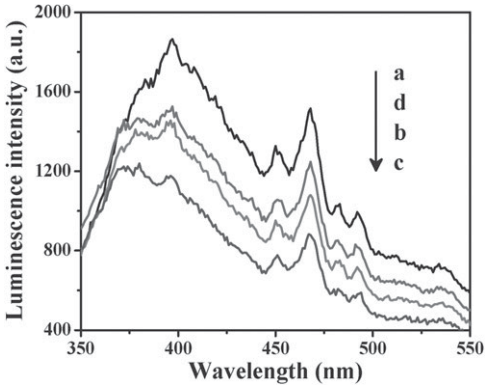

Fig. 10 PL spectra of samples 1 (a), 3 (b), 5 (c) and 6 (d).

as shown in Fig. 10. All the emission spectra shapes are similar and there are five main peaks. The strong peak at about 397 nm is attributed to the emission of band gap transition with the energy of light approximately equal to the bandgap energy of anatase (387.5 nm). The other four small peaks observed in the wavelength range from 440 to 500 nm are attributed to excitonic PL, which mainly result from surface oxygen vacancies and defects. Obviously, compared with pure TiO_2 (sample 1), the intensity of PL signal for the composites (samples 3, 5 and 6) are much lower. There are two main reasons accounting for the decrease in the intensity of PL signal. One is the reduction of the radiative recombination process,[7,15,27,53] that is, the lower the recombination, the weaker the PL signals are. The other is the quenching effect of MWCNTs, that is, some of the generated photoluminescence is absorbed by MWCNTs. In our studies, the former is dominant for sample 3, so the photocatalytic activity is enhanced; the latter is dominant for samples 5 and 6, thus, although samples 5 and 6 have lower PL intensity, they still show inferior activity to sample 1. In this regard, PL analysis in terms of intensity of PL signal, seems to not be a reliable way to monitor the recombination rate in the MWCNTs/TiO_2 composite.

To further support the above proposition, the transient photocurrent responses are recorded for photoelectrodes consisting of pure TiO_2 (sample 1) and MWCNTs/TiO_2 nanocomposites (samples 3 and 5). Fig. 11 shows the *I–t* curves for the three samples with several on-off cycles of intermittent UV-irradiation. It is suggested that the photocurrent is mainly determined by the efficiency of the separation of photo-generated electron-hole pairs within the photoelectrode: holes transfer at the photocatalyst/electrolyte interface, while the electrons are transported to the back contact.[27,54] Normally, as for pristine TiO_2 photocatalysts, the photocurrent curve has an anodic photocurrent spike at the initial time of irradiation. After the spike current has been attained, a continuous decrease in the photocurrent proceeds until a constant photocurrent is reached.[54,55] The photocurrent decay is related to the recombination processes of photo-generated electron-hole pairs. During decay, the holes accumulated at the TiO_2 surface competitively recombine with electrons from the TiO_2 conduction band, instead of being trapped or captured by reduced species in the electrolyte; that is, the decay is largely determined by the efficiency of the transfer of conduction band electrons towards back contact. The photocurrent becomes constant after the equilibration of competitive separation and recombination of electron-hole pairs. In the present study, the photocurrent value rapidly decreases to zero as soon as the UV-light irradiation is switched off, and the photocurrent comes back to a constant value when the light is again switched on (Fig. 11), exhibiting a good reproducibility. Notably, the stable photocurrent value of sample 3 is about 1.2 times as high as that of sample 1. Moreover, for sample 3, the anodic photocurrent spike is relatively not as sharp (compared with sample 1) and is almost equal to the stable photocurrent. These two aspects together suggest less recombination and more efficient separation of photo-generated electron-hole pairs for sample 3 at the interface between MWCNTs and TiO_2.[54,55] Holes diffuse towards the TiO_2 surface, where they are trapped or captured by reduced species in the electrolyte, while the electrons are effectively transported to the back contact *via* the MWCNTs. However, the effective electron transfer depends on the loading amount of MWCNTs: a high MWCNT loading (0.5 wt%, sample 5) results in a less effective separation of photogenerated carrier, and thus lower photocurrent (Fig. 11c).

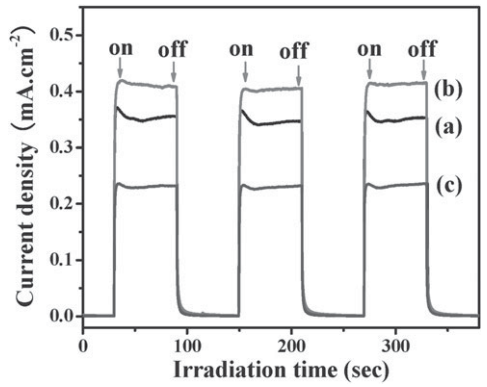

Fig. 11 The transient photocurrent responses of samples 1 (a), 3 (b) and 5 (c) in 1 M Na_2SO_4 aqueous solution under UV light irradiation at 0.5 V *vs.* Ag/AgCl.

4. Conclusions

In this study, we successfully prepare mesoporous multiwalled carbon nanotubes/titanium dioxide (MWCNTs/TiO_2) nanocomposites with low loadings (0–0.5 wt%) of MWCNTs that are mostly embedded inside mesoporous TiO_2 aggregates. Moreover, chemical bonds are formed at the interface between MWCNTs and TiO_2. It is shown that a low MWCNTs loading slightly influences the textural properties and UV-light absorption of the mesoporous TiO_2 aggregates. The dominant factor in enhancing the photocatalytic performance of TiO_2/CNTs composite is identified as the promoted interfacial electron transfer and separation of photogenerated electron-hole pairs at the CNTs/TiO_2 interface. Significantly, we point out that the intensity of PL signal is not a reliable index to reveal the extent of recombination rate in the MWCNTs/TiO_2 composite, due to the quenching effect of CNTs. Alternatively, the analysis of transient photocurrent responses definitely reflects the state of electron transfer and photogenerated

hole-electron separation, which matches well with the changing trend of photocatalytic activity. It clearly indicates that only these chemically-bonded CNTs/TiO_2 composites with appropriate CNT loadings (<0.1 wt%) favor the separation of photo-generated electron-hole pairs and decrease of their recombination rate, and thus display significantly enhanced photocatalytic activity for degrading acetone in air under UV irradiation, as compared with pristine TiO_2 counterparts and commercial P25 photocatalyst. In contrast, a high MWCNT loading (>0.1 wt%) as well as a simple mechanical mixing of MWCNTs and TiO_2, without forming chemical bonds at the interface results in inferior photocatalytic performance because of inhibited interfacial electron transfer and a higher recombination rate of photo-generated electron-hole pairs.

Acknowledgements

This work was partially supported by the National Natural Science Foundation of China (50625208, 20773097, 20877061 and 51072154). This work was also financially supported by the National Basic Research Program of China (2007CB613302 and 2009CB939704) and CHCL09006.

References

1 M. B. McBride, T. J. Pinnavaia and M. M. Mortland, *Adv. Environ. Sci. Technol*., 1977, **8**, 145–154.
2 R. Ekelund, A. Granmo, K. Magnusson, M. Berggren and A. Bergman, *Environ. Pollut*., 1993, **79**, 59–61.
3 C. Karunakaran and S. Senthilvelan, *J. Mol. Catal. A: Chem*., 2005, **233**, 1–8.
4 C. R. Xiong and K. J. Balkus, *J. Phys. Chem. C*, 2007, **111**, 10359–10367.
5 (*a*) M. R. Hoffmann, S. T. Martin, W. Choi and D. W. Bahnemann, *Chem. Rev*., 1995, **95**, 69–96; (*b*) G. Liu, L. Z. Wang, H. G. Yang, H. M. Cheng and G. Q. Lu, *J. Mater. Chem*., 2010, **20**, 831–843.
6 (*a*) J. G. Yu, H. G. Yu, B. Cheng, X. J. Zhao, J. C. Yu and W. K. Ho, *J. Phys. Chem. B*, 2003, **107**, 13871–13879; (*b*) S. W. Liu, J. G. Yu and M. Jaroniec, *J. Am. Chem. Soc*., 2010, **132**, 11914–11916.
7 (*a*) Y. Yu, J. C. Yu, J. G. Yu, Y. C. Kwok, Y. K. Che, J. C. Zhao, L. Ding, W. K. Ge and P. K. Wong, *Appl. Catal., A*, 2005, **289**, 186–196; (*b*) Y. W. Cheng, R. C. Y. Chan and P. K. Wong, *Water Res*., 2007, **41**, 842–852.
8 K. Woan, G. Pyrgiotakis and W. Sigmund, *Adv. Mater*., 2009, **21**, 2233–2239.
9 (*a*) J. C. Yu, J. G. Yu, W. K. Ho, Z. T. Jiang and L. Z. Zhang, *Chem. Mater*., 2002, **14**, 3808–3816; (*b*) C. Trapalis, N. Todorova, M. Anastasescu, C. Anastasescu, M. Stoica, M. Gartner, M. Zaharescu and T. Stoica, *Thin Solid Films*, 2009, **517**, 6243–6247.
10 K. Honda and A. Fujishima, *Nature*, 1972, **238**, 37–38.
11 M. Tomkiewicz, *Catal. Today*, 2000, **58**, 115–123.
12 P. Panagiotopoulou, A. Christodoulakis, D. I. Kondarides and S. Boghosian, *J. Catal*., 2006, **240**, 114–125.
13 (*a*) M. Ksibi, S. Rossignol, J. M. Tatibouet and C. Trapalis, *Mater. Lett*., 2008, **62**, 4204–4206; (*b*) J. G. Yu, Q. J. Xiang and M. H. Zhou, *Appl. Catal., B*, 2009, **90**, 595–602.
14 J. G. Yu, J. F. Xiong, B. Cheng and S. W. Liu, *Appl. Catal., B*, 2005, **60**, 211–221.
15 J. G. Yu, L. Yue, S. W. Liu, B. B. Huang and X. Y. Zhang, *J. Colloid Interface Sci*., 2009, **334**, 58–64.
16 R. Asahi, T. Morikawa, T. Ohwaki, K. Aoki and Y. Taga, *Science*, 2001, **293**, 269.
17 (*a*) J. G. Yu, M. H. Zhou, B. Cheng and X. J. Zhao, *J. Mol. Catal. A: Chem*., 2006, **246**, 176–184; (*b*) S. W. Liu, J. G. Yu and W. G. Wang, *Phys. Chem. Chem. Phys*., 2010, **12**, 12308–12315.
18 J. C. Yu, J. Lin and R. W. M. Kwok, *J. Photochem. Photobiol., A*, 1997, **111**, 199–203.
19 A. Matsumoto, K. Tsutsumi and K. Kaneko, *Langmuir*, 1992, **8**, 2515–2520.
20 T. Hashishin, J. Murashita, A. Joyama and Y. Kaneko, *J. Ceram. Soc. Jpn*., 1998, **106**, 1–5.
21 P. F. Fu, Y. Luan and X. G. Dai, *J. Mol. Catal. A: Chem*., 2004, **221**, 81–88.
22 I. Zhitomirsky, L. Gal-Or, A. Kohn and H. W. Hennicke, *J. Mater. Sci*., 1995, **30**, 5307–5312.
23 M. Inagaki, Y. Nakazawa, M. Hirano, Y. Kobayashi and M. Toyoda, *Int. J. Inorg. Mater*., 2001, **3**, 809–811.
24 B. Tryba, T. Tsumura, M. Janus, A. W. Morawski and M. Inagaki, *Appl. Catal., B*, 2004, **50**, 177–183.
25 S. Iijima, *Nature*, 1991, **354**, 56–58.
26 A. Kongkanand and P. V. Kamat, *ACS Nano*, 2007, **1**, 13–21.
27 H. Yu, X. Quan, S. Chen and H. Zhao, *J. Phys. Chem. C*, 2007, **111**, 12987–12991.
28 B. Gao, G. Z. Chen and G. L. Puma, *Appl. Catal., B*, 2009, **89**, 503–509.
29 S. Muduli, W. Lee, V. Dhas, S. Mujawar, M. Dubey, K. Vijayamohanan, S. H. Han and S. Ogale, *ACS Appl. Mater. Interfaces*, 2009, **1**, 2030–2035.
30 O. Frank, M. Kalbac, L. Kavan, M. Zukalova, J. Prochazka, M. Klementova and L. Dunsch, *Phys. Status Solidi B*, 2007, **244**, 4040–4045.
31 H. Wang, H. L. Wang and W. F. Jiang, *Chemosphere*, 2009, **75**, 1105–1111.
32 A. Jitianu, T. Cacciaguerra, R. Benoit, S. Delpeux, F. Beguin and S. Bonnamy, *Carbon*, 2004, **42**, 1147–1151.
33 B. Liu and H. C. Zeng, *Chem. Mater*., 2008, **20**, 2711–2718.
34 X. H. Xia, Z. J. Jia, Y. Yu, Y. Liang, Z. Wang and L. L. Ma, *Carbon*, 2007, **45**, 717–721.
35 X. B. Yan, B. K. Tay and Y. Yang, *J. Phys. Chem. B*, 2006, **110**, 25844–25849.
36 (*a*) X. H. Li, J. L. Niu, J. Zhang, H. L. Li and Z. F. Liu, *J. Phys. Chem. B*, 2003, **107**, 2453–2458; (*b*) G. H. Xu, Q. Zhang, W. P. Zhou, J. Q. Huang and F. Wei, *Appl. Phys. A: Mater. Sci. Process*., 2008, **92**, 531–539.
37 K. S. W. Sing, D. H. Everett, R. A. W. Haul, L. Moscou, R. A. Pierotti, J. Rouquerol and T. Siemieniewska, *Pure Appl. Chem*., 1985, **57**, 603–619.
38 H. Einaga, T. Ibusuki and S. Futamura, *Environ. Sci. Technol*., 2004, **38**, 285–289.
39 M. H. Zhou, J. G. Yu, S. W. Liu, P. C. Zhai and B. B. Huang, *Appl. Catal., B*, 2009, **89**, 160–166.
40 J. G. Yu, S. W. Liu and M. H. Zhou, *J. Phys. Chem. C*, 2008, **112**, 2050–2057.
41 J. G. Yu, G. H. Wang, B. Cheng and M. H. Zhou, *Appl. Catal., B*, 2007, **69**, 171–180.
42 J. G. Yu, L. J. Zhang, B. Cheng and Y. R. Su, *J. Phys. Chem. C*, 2007, **111**, 10582–10589.
43 J. G. Yu, W. G. Wang, B. Cheng and B. L. Su, *J. Phys. Chem. C*, 2009, **113**, 6743–6750.
44 J. G. Yu, J. C. Yu, M. K. P. Leung, W. K. Ho, B. Cheng, X. J. Zhao and J. C. Zhao, *J. Catal*., 2003, **217**, 69–78.
45 (*a*) Q. H. Yang, P. X. Hou, S. Bai, M. Z. Wang and H. M. Cheng, *Chem. Phys. Lett*., 2001, **345**, 18–24; (*b*) J. G. Yu, H. G. Yu, B. Cheng and C. Trapalis, *J. Mol. Catal. A: Chem*., 2006, **249**, 135–142; (*c*) Q. J. Xiang, K. L. Lv and J. G. Yu, *Appl. Catal., B*, 2010, **96**, 557–564.
46 S. W. Liu, J. G. Yu and S. Mann, *J. Phys. Chem. C*, 2009, **113**, 10712–10717.
47 G. J. Hu, X. F. Meng, X. Y. Feng, Y. F. Ding, S. M. Zhang and M. S. Yang, *J. Mater. Sci*., 2007, **42**, 7162–7170.
48 H. Hiura, T. W. Ebbesen, K. Tanigaki and H. Takahashi, *Chem. Phys. Lett*., 1993, **202**, 509–512.
49 L. Grigorian, K. A. Williams, S. Fang, G. U. Sumanasekera, A. L. Loper, E. C. Dickey, S. J. Pennycook and P. C. Eklund, *Phys. Rev. Lett*., 1998, **80**, 5560–5563.
50 S. Banerjee and S. S. Wong, *Nano Lett*., 2002, **2**, 195–200.
51 J. Li, S. B. Tang, L. Lu and H. C. Zeng, *J. Am. Chem. Soc*., 2007, **129**, 9401–9409.

 This journal is © the Owner Societies 2011

52 Y. J. Xu, Y. B. Zhuang and X. Z. Fu, *J. Phys. Chem. C*, 2010, **114**, 2669–2676.
53 (*a*) Y. Yao, G. Li, S. Ciston, R. M. Lueptow and K. A. Gray, *Environ. Sci. Technol.*, 2008, **42**, 4952–4957; (*b*) Y. Z. Long, Y. Lu, Y. Huang, Y. C. Peng, Y. J. Lu, S. Z. Kang and J. Mu, *J. Phys. Chem. C*, 2009, **113**, 13899–13905.
54 A. Hagfeldt, H. Lindstrom, S. Sodergren and S. Lindquist, *J. Electroanal. Chem.*, 1995, **381**, 39–46.
55 (*a*) J. G. Yu and B. Wang, *Appl. Catal., B*, 2010, **94**, 295–302; (*b*) J. G. Yu, G. P. Dai and B. B. Huang, *J. Phys. Chem. C*, 2009, **113**, 16394–16401; (*c*) B. Gao, C. Peng, G. Z. Chen and G. L. Puma, *Appl. Catal., B*, 2008, **85**, 17–23.

This journal is © the Owner Societies 2011